Robotica (2026), **44**, pp. 2070–2087
doi:10.1017/S0263574726103877

CAMBRIDGE UNIVERSITY PRESS

RESEARCH ARTICLE

Development of extra-long continuum manipulator for nuclear facility inspection

Jung-Che Chang, Jing Liu, Hengtai Dai, Xi Wang, Dragos Axinte and Xin Dong

Faculty of Engineering, University of Nottingham, UK
Corresponding author: Xin Dong; Email: xin.dong@nottingham.ac.uk

Received: 21 March 2026 UTC; **Revised:** 23 July 2026 UTC; **Accepted:** 24 July 2026 UTC

Keywords: serial manipulator design and kinematics; design; redundant manipulators; novel applications of robotics; manufacturing

Abstract

Industrial inspection often requires systems to pass through confined entrances and traverse loosely constrained paths before reaching target locations. Borescopes and long-reach continuum manipulators are susceptible to insertion-induced buckling when deployed without continuous lateral support. This work presents a modular extra-long continuum manipulator designed for such hybrid industrial environments. The system combines a self-recoverable passive body with an independently actuated dual-balloon stabilisation unit, allowing it to traverse regions without continuous lateral confinement and subsequently establish a stabilised lift-up configuration at the target location. Its modular architecture supports transport and field maintenance, while the low-cost disposable design reduces decontamination requirements in harsh or contaminated environments. A solver-free, closed-form framework combines ground, tip, wall-contact, and wrapping resistances to estimate insertion-induced buckling margins for deployment planning. Prototypes (24 mm diameter, 8.2 m length) were validated experimentally and deployed in a nuclear decommissioning hot cell at Nuclear Restoration Services (NRS) Dounreay, UK, carrying a borescope camera and a 70 g radiation sensor to support inspection for subsequent decommissioning decisions.

1. Introduction

Robotic systems offer safer solutions for in-situ inspection and intervention [1, 2]. Many real-world environments – such as civil infrastructure, aeroengines, and pipework systems – require robots to access confined entry points (e.g. narrow gaps [3], aeroengine inspection holes [4]) and operate within more open but cluttered spaces (e.g. isolated rooms [5], aircraft wing and tank [6]). The oil and gas sector demands access to ultra-long confined spaces [7], whereas nuclear [8, 9] and medical [10, 11] applications impose additional constraints such as the need for reliable retrieval and contamination management. Across domains, common challenges include limited accessibility, increased payload demands, and high deployment costs.

Continuum manipulators are increasingly used in the inspection and intervention of high-value infrastructure (e.g. aeroengines [12, 13], aircraft wings [14]) and fragile environments (e.g. living bodies [15], disaster-affected areas [16]). These manipulators are valued for their robustness, structural integrity, relatively high payload capacity, and safe retrieval in failure scenarios. Typically defined as continuously bending structures [17, 18] actuated from the base [19], their development initially focused on miniaturised medical applications [20, 21]. With the slender configuration, they now enable broader use in manufacturing [22], aerospace [23], search and rescue [24], and nuclear industries [25]. As environments grow more complex, requiring higher depth-to-diameter ratios and tighter turns, conventional continuum manipulators face a bottleneck: increasing the number of controllable segments demands more actuators, which enlarges the actuation pack and raises costs and deployment difficulty. Strategies such

© The Author(s), 2026. Published by Cambridge University Press.

Downloaded from https://www.cambridge.org/core. UNIVERSIDAD AUTONOMA METROPOLITANA, on 16 Nov 2026 at 12:10:09, subject to the Cambridge Core terms of use, available at https://www.cambridge.org/core/terms. https://doi.org/10.1017/S0263574726103877

as underactuation [26], special tendon routing [27], and embedded microunits [28] have been explored, but often at the cost of a thicker body.

An alternative approach decouples the number of actuators from the number of bending sections by adopting an endoscope-like insertion strategy [29], where the tip remains steerable although the body passively follows. Active structures have been introduced near the tips of endoscopes and continuum manipulators to enhance this type of design. Locomoting mechanisms such as rolling [30] and worming [31] allow the robot actively moving in the environment, but integration remains a challenge due to the limited access port. In contrast, the concept of creating a stabilising platform through inflation – originally developed for medical applications [32] – has been extended to industrial tasks such as pipework inspection [33], exploration [34], and aeroengine thermal barrier coating repair [35]. However, this strategy relies heavily on the manipulator being laterally supported along its entire insertion path to prevent buckling and ensure anchoring stability. Its functionality becomes significantly limited in environments with alternating narrow and surface-supported regions.

Insertion-induced buckling of slender and continuum manipulators has long been studied within the framework of classical beam theory and elastica formulations, where self-weight buckling and large deflection behaviour are well established through Greenhill-type analysis and Euler–Bernoulli theory [36]. Building on this foundation, more recent studies have focused on modelling insertion mechanics of, catheter-based [37], and continuum manipulators [18] under frictional contact and confinement, often employing Cosserat rod [38, 39] or elastica-based formulations that require solving coupled Ordinary Differential Equations (ODEs), Partial Differential Equations (PDEs), or Nonlinear Programmes (NLPs) to capture large deformation, distributed loading, and contact interactions. These methods can provide detailed predictions of deformation and contact behaviour, but they typically require a numerical solver, a prescribed contact topology, and problem-specific boundary conditions. They are therefore less convenient for rapid path screening during field deployment, particularly when the insertion route contains several distinct contact modes. In the present application, resistance may arise sequentially from distributed ground contact, the end-effector, isolated wall contact, and wrapping around obstacles. This motivates a deployment-oriented assessment framework that combines these resistance contributions within a closed-form calculation and returns a conservative estimate of the insertion force and buckling margin. The framework is intended for rapid feasibility assessment rather than high-fidelity shape prediction.

This paper proposes a low-cost extra-long continuum manipulator with a modular design to overcome the challenges described above:

- A modular continuum-manipulator architecture is developed for hybrid deployment paths comprising a confined entrance, extended surface-supported or loosely constrained regions, and a final elevated inspection task. Unlike systems that depend on continuous lateral confinement, the proposed manipulator can advance across regions without continuous body support and remain safely retrievable.
- A self-recoverable passive body is integrated with an independently actuated dual-balloon stabilisation unit. This configuration separates long-range insertion from distal stabilisation, allowing the manipulator to transition from passive path following to a supported lift-up configuration at the target location.
- A solver-free insertion-stability assessment framework is formulated by combining distributed ground resistance, tip resistance, isolated wall-contact resistance, and wrapping resistance. The framework provides a conservative buckling-margin estimate for rapid structural design and deployment-path screening.

Deployment was successfully demonstrated in a decommissioning nuclear hot cell at Nuclear Restoration Services (NRS) Dounreay, UK. A mock-up trial reflects the entire deployment process. Such inspection challenges frequently arise in large industrial facilities and infrastructure assets, including nuclear decommissioning plants, where access through confined entry points is often required.

Downloaded from https://www.cambridge.org/core. UNIVERSIDAD AUTONOMA METROPOLITANA, on 16 Nov 2026 at 12:10:09, subject to the Cambridge Core terms of use, available at https://www.cambridge.org/core/terms. https://doi.org/10.1017/S0263574726103877

2. Targeted environments and system design

2.1. General environment and system concept

Industrial inspection frequently involves hybrid environments combining narrowly confined entry regions with loosely constrained internal paths. Such hybrid geometries are common in nuclear facilities, pipework systems, and large industrial structures. Access is typically provided through narrow gaps, whereas inspection targets are located across open floor regions, vertical surfaces, or elevated components.

For clarity, the environments considered in this study are classified according to the degree and form of external support. A fully constrained environment continuously supports the manipulator laterally, as in a pipe or narrow channel. A loosely constrained environment provides only partial or intermittent support and may contain several distinct contact modes. These include surface-supported contact, in which the manipulator rests on a horizontal or inclined surface and experiences distributed friction; wall contact, in which a discrete obstacle produces a local reaction and frictional resistance; and wrapping contact, in which the manipulator remains in extended contact with a curved obstacle over a finite wrapping angle. An unconstrained environment refers to a span with no meaningful lateral or surface support. The present stability framework primarily addresses loosely constrained paths containing one or more of the above contact modes.

These conditions create a deployment challenge; a slender device must traverse partially supported paths, transition between different contact modes, and generate elevation without continuous lateral confinement. Conventional insertion strategies, in which only the tip is actively steered and the body passively follows, perform well in fully constrained channels but may become unstable when extended across surface-supported regions without continuous lateral confinement.

To address this class of environments, an extra-long continuum manipulator is proposed (Figure 1). The system comprises three functional sections: an active steering section, a dual-balloon stabilising section incorporating two independently actuated balloon membranes, and a passive compliant body. The two balloon membranes are mounted on opposite sides of a revolute joint and are connected to separate pneumatic supply lines, allowing their inflation pressures to be controlled independently. The slender structure enables navigation through restricted access points, while the stabilising section supports controlled lift-up and sustained positioning in semi-confined spaces. The passive body tolerates environmental contact and recovers from bending, supporting long-reach deployment under loosely constrained environment with practical loading conditions.

2.2. Prototype implementation

Aligning with a low-cost mindset, we prototyped an 8.2 m long manipulator with 3D-printed parts and off-the-shelf components, as shown in Figure 2. The central working channel and section compliance are secured using Polyethylene Terephthalate Glycol-modified (PETG) tubing (outer diameter 12 mm, inner diameter 10 mm). Tubing with maximum length of 1 m is connected, similar to a fishing rod, by rigid 3D-printed connectors for rapid assembly. Guides are fixed to the tubing for cable guidance, while long guides (Figure 2a) appear on both sides of the tubing connector, acting as push-in lockers for the tubing connection. The design also enables the manipulator to be folded (semi-disassembled) into a 1 m bundle, with the electronics and cables readily assembled for convenient delivery and deployment.

The prototype has been built for the inspection of a nuclear decommissioning cell. Borescopes were integrated at the end of the active section and behind the stabilising section, respectively, for visual inspection of the environment and for monitoring the condition of the two balloons in the stabilising section. High-power Light-Emitting Diodes (LEDs) were integrated at the tip and adjacent to the stabilising section to provide sufficient illumination in the dark environment. A 70 g customised online radiation sensor is mounted in the general sensor chassis for observing radiation readiness. The 10 mm hollow working channel from the tubing secures the cable connections of the electronics, which are all linked to the actuation pack of the manipulator and connected to the corresponding devices.

Downloaded from https://www.cambridge.org/core. UNIVERSIDAD AUTONOMA METROPOLITANA, on 16 Nov 2026 at 12:10:09, subject to the Cambridge Core terms of use, available at https://www.cambridge.org/core/terms. https://doi.org/10.1017/S0263574726103877

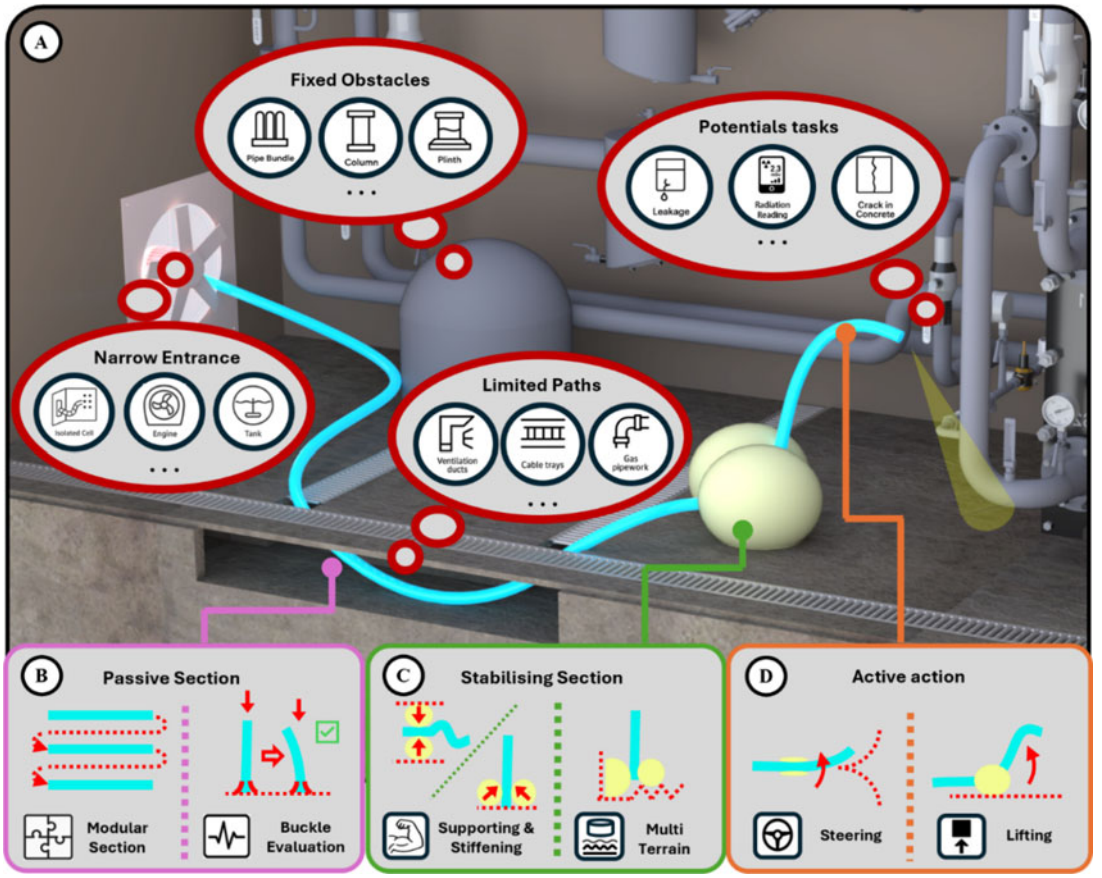


Figure 1. *Schematic of the extra-long continuum manipulator. a: General use case, b: Function of passive section, c: Function of stabilising section, and d: Function of the active section.*

The active section consists of a fine adjustment tip and a steerable head. Being covered by a cable sleeve, the fine adjustment tip (outer diameter 24 mm), with a 3D-printed (Tough 2000, Formlabs) pivot joint design [4], enables 2-Degrees of Freedom (DoF) bending motion with 110° bending angle, allowing the front borescope to point in the desired direction with a small bending radius. The steerable head, made of PETG tubing, provides sufficient stiffness to enable navigation by engaging with the environment.

The stabilising section incorporates a revolute joint that releases the reaction moment generated by the deformed passive body during the lift-up motion. A four-bar linkage minimises the restoring moment of the joint while maintaining a mechanically constrained configuration during insertion. Two balloon membranes are mounted on opposite sides of the revolute joint and connected to separate pneumatic supply lines, enabling independent inflation and deflation.

When both balloons are deflated, their membranes remain tensioned around the joint and work with the mechanical stops to restrict unintended rotation during navigation. Once the stabilising section reaches the target location, the two balloons are inflated through their respective pneumatic lines to establish support against the surrounding structure. Their pressures can be adjusted independently to accommodate asymmetric contact conditions and to stabilise the revolute joint during the subsequent lift-up motion.

Downloaded from https://www.cambridge.org/core. UNIVERSIDAD AUTONOMA METROPOLITANA, on 16 Nov 2026 at 12:10:09, subject to the Cambridge Core terms of use, available at https://www.cambridge.org/core/terms. https://doi.org/10.1017/S0263574726103877

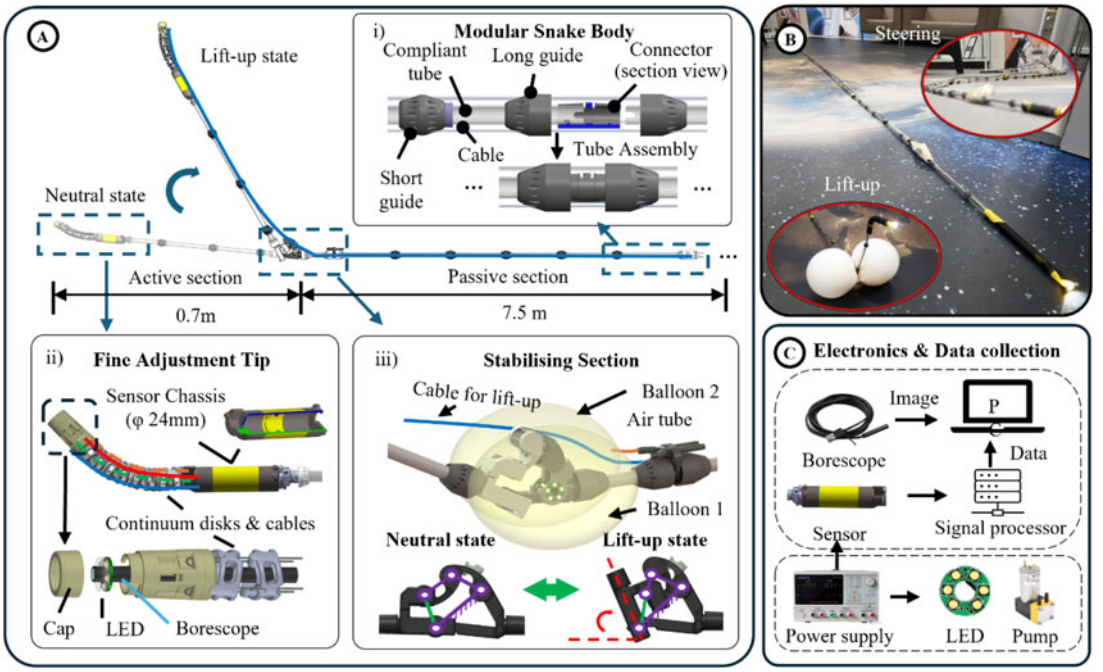


Figure 2. *Prototype of the extra-long continuum manipulator. a: Design of the prototype, b: Prototype figure, and c: Integrated electronics.*

3. Insertion stability assessment framework

Long-reach deployment requires estimating whether the manipulator can reach the target location without insertion-induced buckling. This section develops an assessment method to support:

1. Selection of structural stiffness during design.
2. Evaluation of allowable navigation depth during deployment planning.

The objective is to provide a conservative stability bound for practical decision-making.

3.1. Navigation distance on under surface-supported contact

This section considers a surface-supported contact condition within a loosely constrained environment. The manipulator rests on a supporting surface and is advanced approximately along its longitudinal axis without continuous lateral confinement. Insertion-induced buckling is assumed to initiate near the proximal boundary of the unsupported or weakly supported span. The principal axial resistances are the distributed friction generated by the body weight F_s and the frictional resistance at the end-effector F_{tip}. Defining the beam material density ρ and the cross-sectional area A, F_s and F_{tip} can be respectively described through the Coulomb coefficient μ_{body} and μ_{tip} is expressed as:

$$\begin{cases} F_s(x) = \mu_{body}\rho A g\,(l_{max} - x) \\ F_{tip} = \mu_{tip} m_{tip} g \end{cases} \tag{1}$$

where m_{tip} is the mass of the integrated end-effector; l_{max} is the maximum length of the beam before buckling; g is the gravitational acceleration; and x is the position along the beam.

Downloaded from https://www.cambridge.org/core. UNIVERSIDAD AUTONOMA METROPOLITANA, on 16 Nov 2026 at 12:10:09, subject to the Cambridge Core terms of use, available at https://www.cambridge.org/core/terms. https://doi.org/10.1017/S0263574726103877

The situation can be simplified as a Euler–Bernoulli cantilever beam, and the equilibrium (critical state) for buckling can be expressed as:

$$EI\frac{d^4y(x)}{dx^4} + (F_{\text{tip}} + F_s(x))\frac{d^2y(x)}{dx^2} = 0 \tag{2}$$

where E is the Young's modulus of the beam; I is the second moment of inertia of the beam; and y is the beam deflection.

By a change of variable $z = (l_{\max} - x) + F_{\text{tip}}/(\mu_{\text{body}}\rho Ag)$, the equation reduces to the classical Greenhill self-buckling challenge [40] with an unloaded effective length $l_0 = l_{\max} + F_{\text{tip}}/(\mu_{\text{body}}\rho Ag)$, leading to a maximum beam length:

$$l_{\max} = l_0 - \frac{F_{\text{tip}}}{\mu_{\text{body}}\rho Ag} \tag{3}$$

where l_0, based on the Greenhill challenge, can be expressed as:

$$l_0 \approx \left(\frac{CEI}{\mu_{\text{body}}\rho Ag}\right)^{\frac{1}{3}} \tag{4}$$

where the numerical coefficient $C = 7.8373$ corresponds to the first dimensionless eigenvalue of the classical Greenhill self-weight buckling problem. It encapsulates the effect of distributed axial compression and boundary conditions on the onset of instability, rather than representing a material parameter.

Hence, leading to a conclusion:

$$l_{\max} \approx \left(\frac{CEI}{\mu_{\text{body}}\rho Ag}\right)^{\frac{1}{3}} - \frac{\mu_{\text{tip}}m_{\text{tip}}}{\mu_{\text{body}}\rho A} \tag{5}$$

As a result, Eq. (5) therefore provides a closed-form upper bound for the maximum insertion length under surface-supported contact. It offers a direct design criterion linking material stiffness, cross-sectional geometry, distributed surface friction, and tip resistance to the onset of insertion-induced buckling.

3.2. Buckling assessment along a hybrid contact path

A loosely constrained deployment path may contain several sequential contact modes. For the present assessment, the corresponding insertion resistance F_{sum} is decomposed into four contributions:

1. Ground resistance F_s: distributed friction arising from surface-supported contact along the manipulator body, derived in Eq. (1);
2. Tip resistance F_{tip}: frictional resistance acting at the end-effector, derived in Eq. (1);
3. Wall resistance F_{wall}: local friction generated when the manipulator is deflected against a discrete wall or obstacle.
4. Wrapping resistance: force-transmission loss generated when the manipulator remains in continuous contact with a curved obstacle, such as a plinth or column, over a known wrapping angle ϕ;

where the last condition complies with the capstan friction formula [41]. Defining F_{out} as the force leaving the segment on the distal side, and F_{in} as the force entering the wrapping segment from the proximal side, the force approximates an exponential relationship under the Coulomb friction coefficient μ_c, expressed as:

$$F_{\text{out}} = F_{\text{in}}e^{-\mu_c\phi} \tag{6}$$

The hybrid path is divided into segments according to the locations of the wrapping contacts. The resistance generated in each distal segment is propagated towards the proximal actuation end using the

Downloaded from https://www.cambridge.org/core. UNIVERSIDAD AUTONOMA METROPOLITANA, on 16 Nov 2026 at 12:10:09, subject to the Cambridge Core terms of use, available at https://www.cambridge.org/core/terms. https://doi.org/10.1017/S0263574724103877

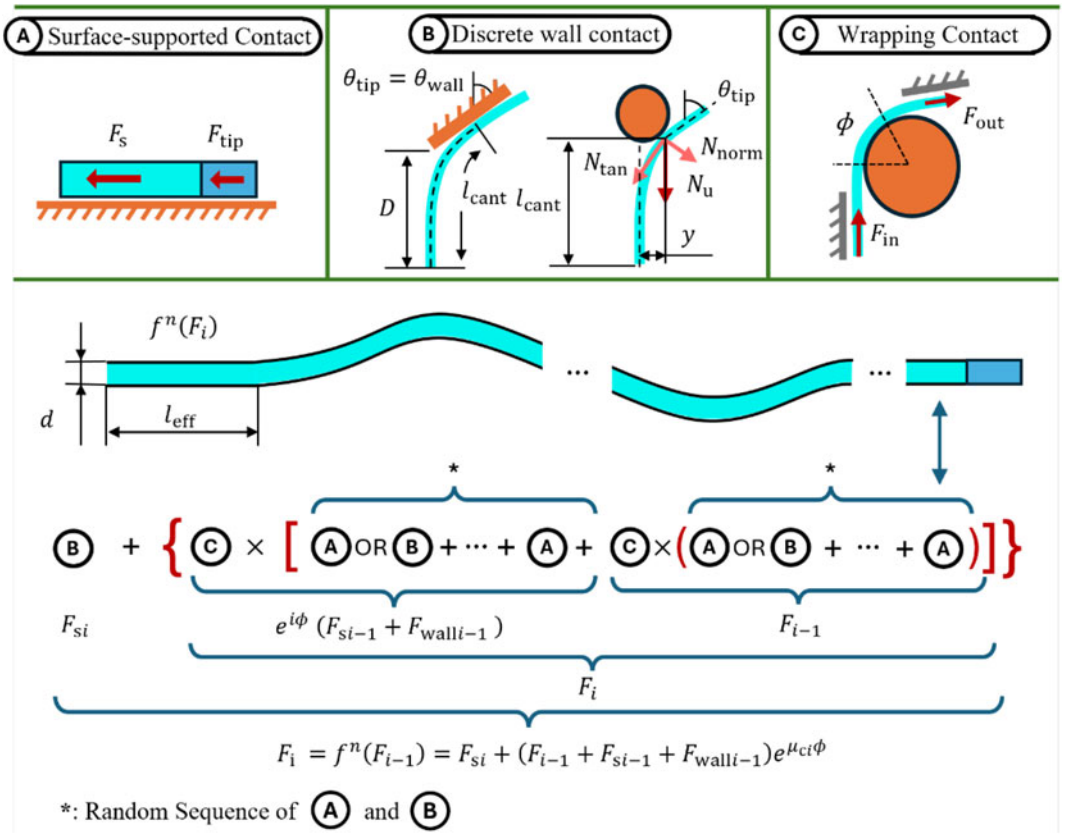


Figure 3. *Contact modes considered in the insertion-stability assessment. a: Surface-supported contact with distributed ground and tip resistance, b: Discrete wall contact, and c: Wrapping contact around a curved obstacle.*

inverse capstan relation. By segmenting the environment through wrapping, the transferred resistance $F_i = f(F_{i-1})$ after the number i wrapping resistance (count from the head of the manipulator) can be expressed as:

$$F_i = F_{si} + (F_{i-1} + F_{si-1} + F_{wall\,i-1})e^{\mu_{ci}\phi} \tag{7}$$

Accordingly, each wrapping segment increases the proximal force required to overcome the resistance located beyond that segment. The positive exponent used in Eq. (7) therefore represents inverse force propagation for calculating the required actuation force; it does not represent physical force amplification across the contact.

Defining the effective beam length l_{eff} and the column effective length coefficient $K = 2$ for the case of a cantilever beam, the buckling discriminant can be expressed as:

$$F_{sum} = f^n(F_i) \geq F_{cr} = \frac{\pi^2 EI}{(Kl_{eff})^2} \tag{8}$$

where $i = 0, 1, \ldots, n-1$ is the number of the wrapping resistance counting from the head of the manipulator.

With Coulomb friction coefficient μ_{wall} for the wall, the wall resistance can be expressed as:

$$F_{wall} = \mu_{wall} N_{norm} + N_{axis} \tag{9}$$

where N_{norm} is the support reaction from the beam deformed by the wall (Figure 3).

Downloaded from https://www.cambridge.org/core. UNIVERSIDAD AUTONOMA METROPOLITANA, on 16 Nov 2026 at 12:10:09, subject to the Cambridge Core terms of use, available at https://www.cambridge.org/core/terms. https://doi.org/10.1017/S0263574726103877

To account for large deformations, we employed the elastica formulation and used a fifth-order Taylor expansion [42] as an approximate solution. The force along the normal direction of the unbent body N_u (Figure 3) can be expressed as:

$$N_u \approx N_0 \left(1 + \frac{9y^2}{35{l_{cant}}^2} + \frac{2358y^4}{13475{l_{cant}}^4}\right) \tag{10}$$

where l_{cant} is the effective length of the cantilever beam, and N_0 is the linear term corresponding to the Euler–Bernoulli prediction [40], expressed as:

$$N_0 = \frac{3EI}{{l_{cant}}^3} y \tag{11}$$

For large deformation, the tip angle θ_{tip} is significant. Therefore, the correlation between N_u and N_{norm} can be expressed as:

$$\begin{cases} N_{norm} = N_u \cos\theta_{tip} \\ N_{axis} = N_u \sin\theta_{tip} \end{cases} \tag{12}$$

where N_{axis} is the force along the tangent direction of N_{norm}.

The tip angle θ_{tip} can be obtained in the same manner by a fifth-order Taylor expansion, expressed as:

$$\theta_{tip} \approx \frac{N_u {l_{cant}}^2}{2EI} + \frac{{N_u}^3 {l_{cant}}^6}{24E^3I^3} + \frac{3{N_u}^5 {l_{cant}}^{10}}{40E^5I^5} \tag{13}$$

substituting the N_u into θ_{tip}, the result can be expressed as:

$$\theta_{tip} \approx \frac{3y}{2l_{cant}} \left(1 + \frac{75y^2}{112{l_{cant}}^2} + \frac{6379767y^4}{689920{l_{cant}}^4}\right) \tag{14}$$

For each wall-contact configuration, l_{cant} and y are obtained directly from the prescribed obstacle geometry, and θ_{tip} is evaluated using the fifth-order beam approximation. These quantities are then used to calculate N_u, after which N_{norm} and N_{axis} are obtained by resolving the force relative to the wall-contact direction. The calibrated wall-contact coefficient is finally applied to calculate the corresponding frictional resistance.

In summary, Eq. (5) estimates the maximum insertion length for the baseline surface-supported contact condition. A loosely constrained hybrid path may additionally contain discrete wall-contact and wrapping-contact segments. The resistance associated with each segment is evaluated according to its contact mode and propagated towards the actuation end using Eq. (7). The resulting proximal insertion-force demand is then compared with the critical buckling load through the discriminant as in Eq. (8).

4. Framework validation under controlled testbeds

4.1. Validation of the critical insertion length under surface-supported contact

This experiment validates the baseline surface-supported contact model developed in Section 3.1. The test reproduces distributed friction along the rod while excluding discrete wall-contact and wrapping-contact effects. The resulting critical insertion length provides a baseline criterion for selecting the manipulator stiffness and estimating the allowable insertion distance before deployment.

The critical buckling length can guide the design of the manipulator, ensuring that the effective insertion length eventually reaches the target depth after navigation. A scaled-down dummy test has been conducted to prove the effectiveness of the modelling. The validation focuses on straight horizontal insertion, which provides a baseline for the initial design of the manipulator prototype. As shown in Figure 4, to maximise the distributed friction along the length, we sandwiched the rods between rubber sheets. The rubber sheets were fixed on rigid boards and pressed by two clamps, with the height controlled by spacers placed at the corners and edges of the boards. 3D printing filaments were chosen as the testing rods, and the straightness was mechanically improved at room temperature. To distinguish

Downloaded from https://www.cambridge.org/core. UNIVERSIDAD AUTONOMA METROPOLITANA, on 16 Nov 2026 at 12:10:09, subject to the Cambridge Core terms of use, available at https://www.cambridge.org/core/terms. https://doi.org/10.1017/S0263574726103877

Table I. *List of the test rod.*

Material	Diameter (mm)	Young's modulus (MPa)
PLA Tough	2.77	2,797 ± 151
Polylactic Acid (PLA)	2.75	3,250 ± 119
Acrylonitrile Butadiene Styrene (ABS)	1.74	2000 ± 100 MPa
PETG	1.69	1610 ± 130 MPa

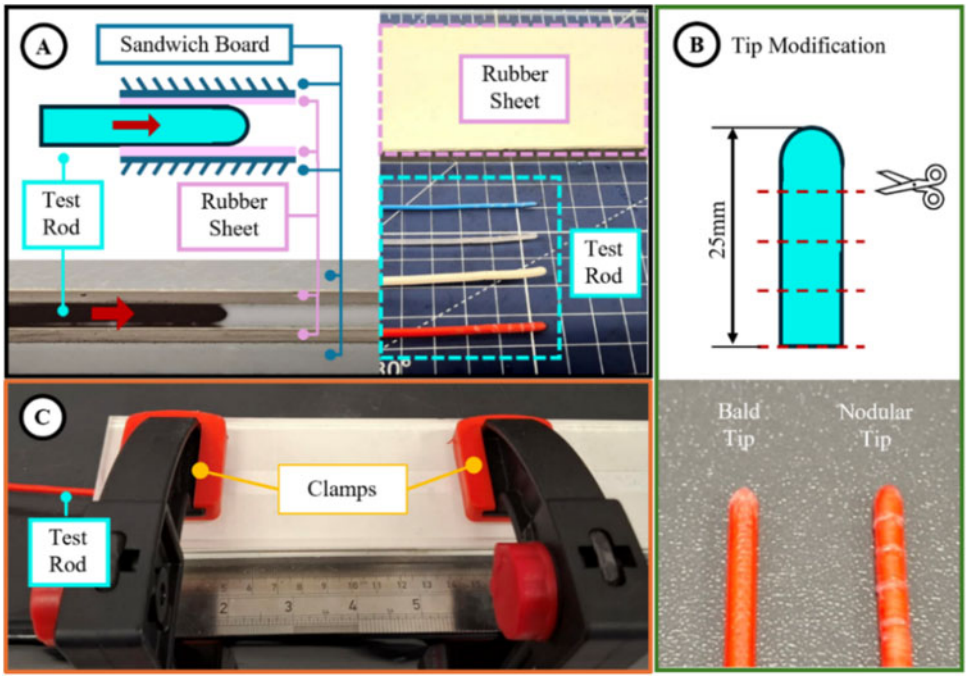


Figure 4. *Preparation for the critical buckling length test. a: Setup configuration, component, and test rods to be inserted, b: Tip modification for friction coefficient variation, and c: Test setup.*

the friction between the manipulator tip and the manipulator body, tip modification was carried out by applying ring carvings at the tip of the rods to vary the friction coefficient.

Four different rods were selected for the validation test. The diameters are measured from a caliper, and the Young's modulus was obtained from the product data sheet. The specification is listed in Table I.

By introducing the body line friction density $F_s^{'}$ and tip friction density $F_{tip}^{'}$, l_{max} in Eq. (5) can be rewritten as:

$$l_{max} \approx \left(7.8373 \frac{EI_{rod}}{F_s^{'}}\right)^{\frac{1}{3}} - \frac{F_{tip}^{'}}{F_s^{'}} \tag{15}$$

where $I_{rod} = \frac{\pi}{64} D_{rod}{}^4$ is the cross-sectional moment of the inertia, and D_{rod} is the diameter of the rod.

Before the critical-buckling-length tests, the friction parameters of each rod material were calibrated once using the same rubber-sheet configuration. During calibration, the rod was inserted through the complete length of the rubber sheets and allowed to protrude from the opposite end. This arrangement ensured that, when the rod was pulled using the dynamometer, the full length of the rubber-sheet contact region corresponded to the line-friction calculation length.

Downloaded from https://www.cambridge.org/core. UNIVERSIDAD AUTONOMA METROPOLITANA, on 16 Nov 2026 at 12:10:09, subject to the Cambridge Core terms of use , available at https://www.cambridge.org/core/terms. https://doi.org/10.1017/S0263574726103877

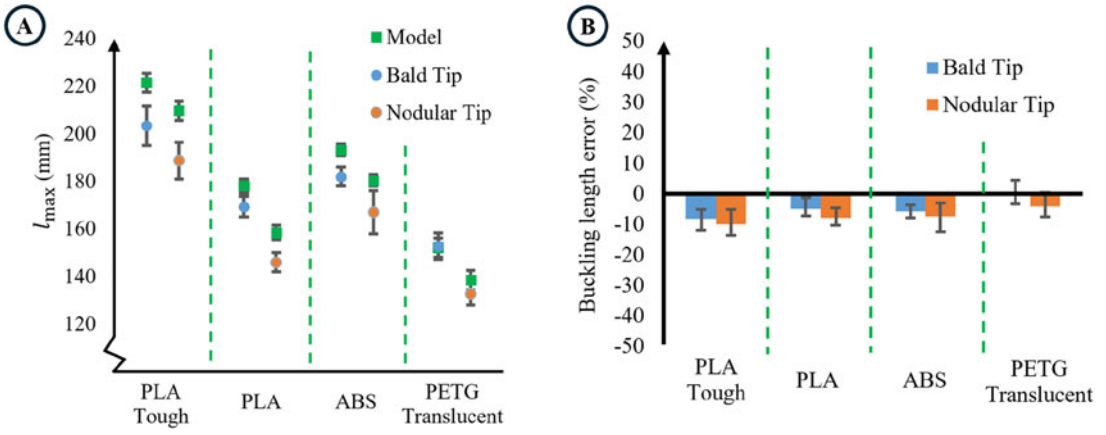


Figure 5. *Result of the critical bulckling length test. a: Test results and b: Errors.*

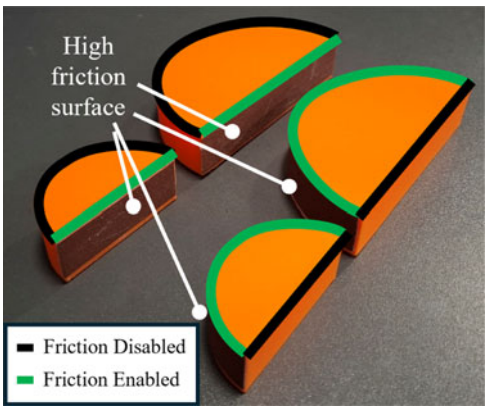


Figure 6. *Objects for the test setup. Additional surface is locally attached for a considerable friction.*

The pulling force was first measured using the reference rod tip to identify the distributed body friction over the known contact length. The resulting body line-friction density was calculated by dividing the measured distributed resistance by the rubber-sheet contact length. A second measurement was then conducted using the modified nodular tip. After subtracting the distributed body-friction contribution, the remaining force was attributed to the tip resistance. The resulting calibrated F_s' were 5.88, 9.898, 1.176, and 1.47N/mm for PLA Tough, PLA, ABS, and PETG, respectively. The corresponding F_{tip}' were 6.86, 12.74, 2.45, and 1.96 N/mm, respectively. These calibrated values were used in Eq. (15) without further adjustment when predicting the critical insertion length for each material.

The tested result and error are shown in Figure 5. By pulling rods out from the rubber sheets under specific length (20 mm for bald tips and 100 mm for nodular tip), the resistance was measured through a dynamometer. The insertion length of the corresponding material was then tested to keep a consist rubber sheet height. The maximum insertion length for each type of rod was tested three times, and error bar was obtained considering both the deviation of the tested length and the error from the supplied Young's modulus. The results should not be compared directly across materials because the applied friction conditions differed between the tests.

4.2. Validation of resistance

Friction tests were conducted using the same rods. As shown in Figure 6, semi-circular objects (diameter 30 and 60 mm) fabricated by 3D printing were used as obstacles and fixed onto the tabletop. Treating

Downloaded from https://www.cambridge.org/core. UNIVERSIDAD AUTONOMA METROPOLITANA, on 16 Nov 2026 at 12:10:09, subject to the Cambridge Core terms of use, available at https://www.cambridge.org/core/terms. https://doi.org/10.1017/S0263574726103877

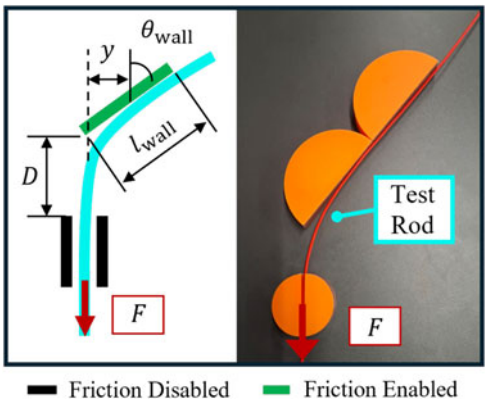


Figure 7. *Setup for the discrete wall contact resistance test. The rod interacts with an inclined wall at angle θ, and the resulting axial force is measured to quantify frictional contact effects.*

the friction from the object surface negligible (friction disabled), we use fine coarse paper as high friction surface to attach at the object surface to enable significant friction. The rod was bent within the environment to conform to the obstacles, and the rod was pulled backwards from the bottom using a dynamometer to measure the tensile force.

Contact resistance and wrapping resistance were tested respectively in two setups. To prevent mechanical jamming, a clearance of 0.5–1 mm was introduced in all setups relative to the theoretical dimensions. For the contact resistance setup, the rod was in contact with an inclined flat wall to evaluate the axial force induced by wall friction (Figure 7). The starting point of the wall was aligned with the vertical extension line of the rod. The wall inclination angle θ_{wall} is the controlled variable. The distance D between the starting point of the wall and the numerical constraint endpoint of the rod, and the wall length l_{wall} were set as constant.

In the resistance-validation experiments, the rod was pulled from the proximal side using a dynamometer, whereas the resisting contact force was generated distally by the wall or wrapping fixture. The measured dynamometer force therefore corresponds to the proximal force required to overcome a known distal resistance. Consequently, the experimental prediction uses the inverse form of the capstan relation:

$$F_{wall} = \mu_{wall} N_{norm} - N_{axis} \tag{16}$$

rather than the forward transmission form in Eq. (6). The positive exponent reflects the direction in which the required force is calculated and does not imply force generation by the wrapping contact.

For each tested material, the wall-contact friction coefficient μ_{wall} was calibrated using the measured pulling force at the reference wall inclination of $\mu_{wall} = 40°$. The geometric parameters l_{cant}, y, and θ_{tip} were first obtained from the prescribed test geometry following the procedure described in Section 3.2. The measured pulling force at 40° was then substituted into Eqs. (9)–(14), and the equations were rearranged to determine μ_{wall}. Using the reference condition $\mu_{wall} = 40°$, the calibrated wall-contact friction coefficients were 1.46, 1.42, 1.37, and 1.4 for PLA Tough, PLA, ABS, and PETG, respectively. These coefficients were then held constant when predicting the pulling forces at the remaining wall inclination angles.

The tested result is shown in Figure 8. To keep the resistance within a measurable range, $l_{wall} =$ 120 mm was set for all the tests, $D = 60$ mm for PLA tough and PLA, and $D = 30$ mm for ABS and PETG. l_{cant} and y can be obtained based on constant curvature assumption. It should be noted that the results are not intended for direct inter-material comparison because the geometric distance D differed between the tests.

The wrapping contact resistance experiment (Figure 9) examined the relationship between the wrapping angle and the force required to transmit a prescribed distal resistance through the contact. The

Downloaded from https://www.cambridge.org/core. UNIVERSIDAD AUTONOMA METROPOLITANA, on 16 Nov 2026 at 12:10:09, subject to the Cambridge Core terms of use, available at https://www.cambridge.org/core/terms. https://doi.org/10.1017/S0263574726103877

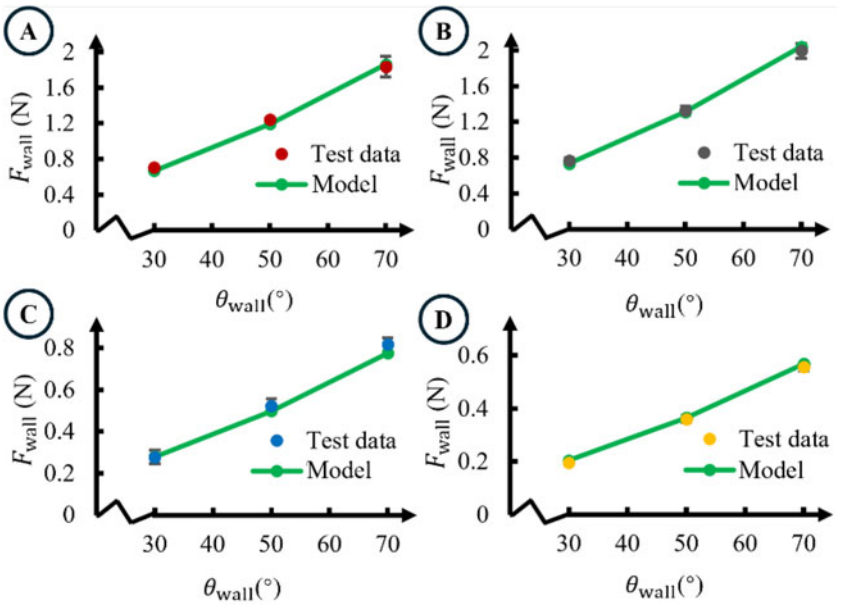


Figure 8. *Result of the contact resistance test with different materials. a: Result of PLA tough, b: Result of PLA, c: Result of ABS, and d: Result of PETG.*

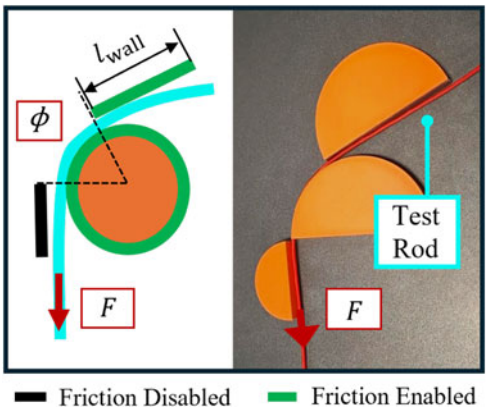


Figure 9. *Setup for the wrapping contact resistance test. The rod wraps around a cylinder with controlled angle ∅, and the transmitted tensile force is measured to assess friction loss.*

straight frictional wall generated the distal resistance, while the dynamometer measured the corresponding proximal pulling force. The cylindrical obstacle was positioned tangentially to the straight wall, and its angular position defined the angle ϕ, which is also the wrapping angle of the rod.

PLA tough was selected as the tested material and the result is shown in Figure 10. $l_{\text{wall}} = 60$ mm was set for the test. The wrapping-contact coefficient μ_c was calibrated using the measured forces at the reference wrapping angle of $\phi = 20°$ and disabled wall contact resistance. The force measured without friction on the cylindrical surface was taken as the reference distal force F_{out}, while the dynamometer reading obtained with the frictional wrapping surface provided the corresponding proximal pulling force F_{in}. The coefficient was calculated by rearranging the inverse capstan relation:

$$\mu_c = \ln(F_{in}/F_{out})/\phi \tag{17}$$

Downloaded from https://www.cambridge.org/core. UNIVERSIDAD AUTONOMA METROPOLITANA, on 16 Nov 2026 at 12:10:09, subject to the Cambridge Core terms of use, available at https://www.cambridge.org/core/terms. https://doi.org/10.1017/S0263574726103877

Table II. *Specifications of the implemented extra-long continuum manipulator.*

Parameter	Specification
Total length	8.2 m
Total mass	<2 kg
Segment lengths	Up to 1 m
Section diameters	25 mm
Bending ranges	∼±110°
Actuation method	Cable driven
Cable numbers	9 driving cables in total
Pressure limits	Below 2 bars
Payload limits	Below 120 g

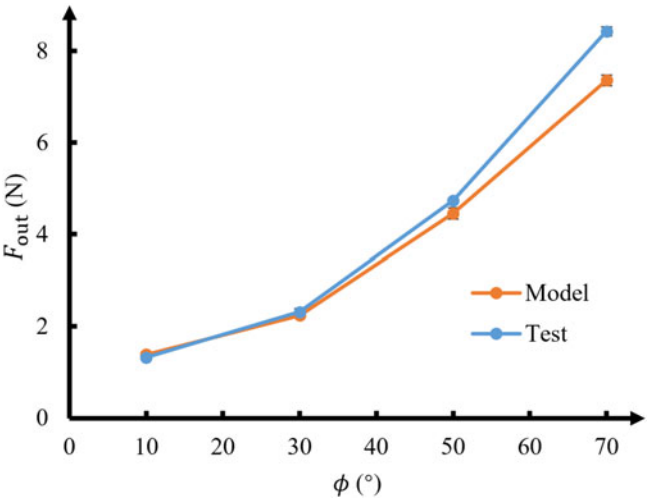


Figure 10. *Result of the wrapping resistance test.*

The value identified at $\phi = 20°$ was subsequently used without further adjustment to predict the pulling force at the remaining wrapping angles. Using the reference wrapping angle $\phi = 20°$, the calibrated wrapping-contact friction coefficient for the PLA Tough rod was 1.03. The wrapping angle was expressed in radians when evaluating the capstan relation. This calibrated coefficient was used without further adjustment to predict the proximal pulling force at the remaining wrapping angles.

The loss-free tensile force was directly measured experimentally when the cylindrical object was not covered with sandpaper.

Each experimental condition in the wall-contact and wrapping-contact tests was repeated three times. The values presented in Figures 8 and 10 are the mean measured forces, and the error bars represent the variability across the three repeated measurements. The maximum error-bar magnitude among all reported conditions was 0.16 N. Because this value is small relative to the force ranges shown in the figures, several error bars are not readily distinguishable at the plotted scale.

5. Field-representative mock-up testing and in-field deployment

The manipulator described in Section 2 has been deployed in a nuclear decommissioning cell at NRS Dounreay for vision and radiation inspection. Before deployment in the active environment, full-scale mockup tests were conducted to verify the deployment procedure and train the site engineers. The mockup has been setup based on the supplied drawing and the feedback from Dounreay engineers. Table II summarises the key specification of the prototyped manipulator.

Downloaded from https://www.cambridge.org/core. UNIVERSIDAD AUTONOMA METROPOLITANA, on 16 Nov 2026 at 12:10:09, subject to the Cambridge Core terms of use, available at https://www.cambridge.org/core/terms. https://doi.org/10.1017/S0263574726103877

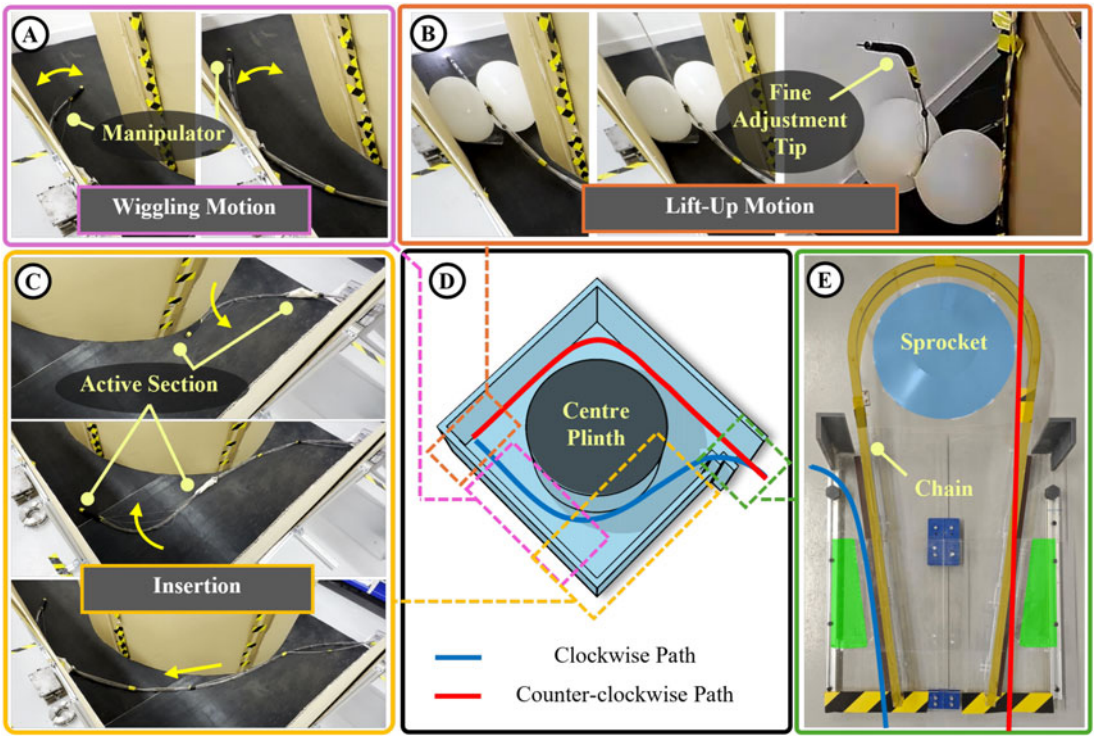


Figure 11. *Setup and deployment in the mockup. a: Manipulator wiggling motion for compression stress releasing, b: Lift-up motion at the target location, c: Manipulator key posture during insertion, d: Arrangement of the mockup, and e: Entrance of the mockup.*

5.1. Field-representative mock-up testing

As shown in Figure 11, the mockup reconstructed the configuration of the inspecting cell and facilities that will potentially interact with the manipulator during the deployment. The cell is around 3.5 m $\times$ 3.5 m and the maximum travelling distance is around 7.5 m. The cell consists of a $\sim\phi$2 m plinth to support a $\sim\phi$3 m turning table seating right above and previously being controlled with a motor transmitted through a chain and sprocket. By taking the worst condition, the friction of the ground surface was increased by placing an anti-slippery rubber mat on the floor. As the first step of the deployment, the manipulator is required to pass through the gap between the chain and wall referred to as the entrance. The entrance configuration (Figure 11d) comprises a chain-driven sprocket system positioned close to the cell wall, with angle irons and bolted structural elements forming a narrow and partially constrained access gap.

The manipulator accessed the cell through gaps between the chain and the concrete wall, covering the whole ground floor inspection through a clockwise and a counter-clockwise path. While the counter-clockwise path requires a longer travelling distance and slightly tighter gap to climb over the chain and navigate into the cell (red path in Figure 11d), the clockwise path holds a larger challenge with more bends, which is the risk of causing insertion-induced buckling.

On the clockwise path, the manipulator enters through the gap between the lower-side chain (blue path in Figure 11d) and the side wall. Before reaching the angle iron, the manipulator left bent its fine adjustment, which provides effective steering within confined space where requires small bending radius. By keeping feed-in the body of the manipulator after the left turn, the manipulator enters the interior of the cell. The active section then provided a left steering (Figure 11c), offering a 4.5 times larger searching area compared with the steering from the fine adjustment tip. This allows the manipulator to reach the centre plinth and passively guide the body leftwards and finally reach bottom corner. The active section

Downloaded from https://www.cambridge.org/core. UNIVERSIDAD AUTONOMA METROPOLITANA, on 16 Nov 2026 at 12:10:09, subject to the Cambridge Core terms of use, available at https://www.cambridge.org/core/terms. https://doi.org/10.1017/S0263574726103877

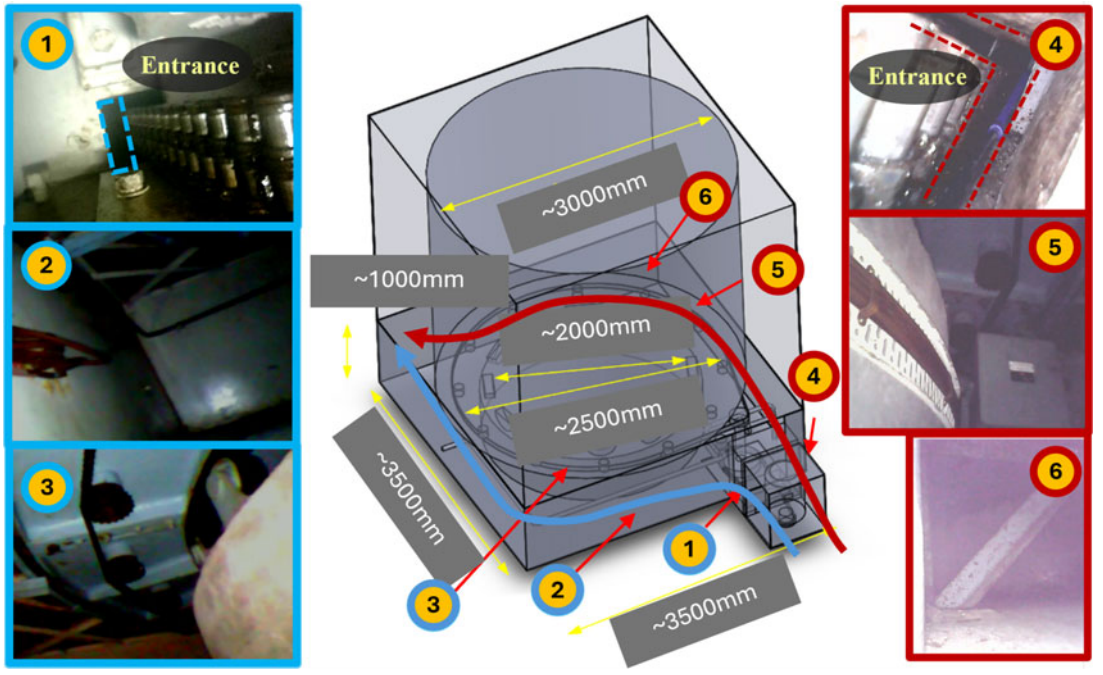


Figure 12. *Deployment in a real nuclear hot cell. Images 1–6 are have been captured by the camera mounted in the manipulator. The left and right entrances are marked in blue and red dashed lines.*

of advancing the manipulator was then prepared for the coming contact with the wall of the cell (middle figure in Figure 11d).

Further advancement enables the manipulator to utilise the supporting force from the wall to guide its body to bend, as illustrated in Figure 11d. However, when manipulator receives a large payload which approaches the theoretical limit, the manufacturing imperfection of the manipulator structure still leads to insufficient axial stiffness, which can no longer transmit the feed-in force effectively, leading to an insertion-induced buckling failure.

Wiggling the manipulator's head during the feed-in can push the actual buckling condition closer to the theoretical situation (Figure 11a). This motion converts static friction into dynamic friction while releasing the elastic potential energy stored in the body, thereby relieving the stress accumulation over the body section. The body section achieves a nearly 90° bend after repeating several times of the wiggling. Continued advancement then allows the manipulator to reach the target position, ready for the lift-up motion and further inspection.

5.2. In-field deployment

Following te mock-up training, five deployments were conducted independently by the Dounreay engineering team in the active nuclear cell (Figure 12 – Images 1–6 are some of the video crops taken from the front borescope). Thanks to the higher power LED, the illumination lights up the fully dark environment and provides sufficient brightness for vision inspection.

All five deployments completed their planned operational objectives. The system required no more than 20 min for on-site assembly and preparation. Each insertion, inspection, and data-collection operation were completed within 20 min.

A deployment was classified as successful when the manipulator reached the planned target region, established a stable inspection configuration, acquired the required sensor data, and was subsequently retrieved without structural damage or operational intervention inside the cell.

Downloaded from https://www.cambridge.org/core. UNIVERSIDAD AUTONOMA METROPOLITANA, on 16 Nov 2026 at 12:10:09, subject to the Cambridge Core terms of use, available at https://www.cambridge.org/core/terms. https://doi.org/10.1017/S0263574726103877

Approximately 7.5 m of the 8.2 m manipulator was inserted during the longest deployment. At the target location, the stabilising section supported a lift-up height of approximately 0.67 m while carrying the borescope and the 70 g radiation sensor. No loss of retrieval capability, structural failure, or unrecoverable buckling occurred during the five active-cell deployments.

Before active-cell deployment, the stability framework was applied to the representative mock-up paths using the estimated insertion length, contact sequence, and resistance parameters. Paths for which the estimated proximal insertion-force demand remained below the predicted buckling limit were classified as feasible. Path configurations approaching or exceeding the predicted limit were treated as high risk and were either modified or excluded from the active-cell procedure.

The selected feasible paths were subsequently completed successfully in the mock-up and during the five active-cell deployments. This outcome provides practical corroboration that the framework was suitable for conservative path screening. However, deliberate deployment along paths classified as high risk was not permitted because an insertion-induced buckling failure could have compromised retrieval and contamination control. The field trials therefore verify successful operation within the predicted feasible region but do not constitute a controlled validation of both feasible and infeasible path classifications.

6. Discussion and conclusion

This work presented a modular extra-long continuum manipulator for hybrid deployment paths containing confined entrances, surface-supported or loosely constrained regions, and an elevated inspection target. The principal system-level contribution is the separation of long-range insertion from local lift-up stabilisation: the self-recoverable passive body permits advancement without continuous lateral confinement, while the independently actuated dual-balloon unit is activated at the target to support the lift-up operation. The contribution therefore extends beyond increasing the available reach or adapting an existing manipulator to a nuclear environment.

The second contribution is a deployment-oriented, solver-free stability assessment that combines the principal resistance modes encountered along a hybrid path. Rather than predicting the complete deformed configuration, the framework estimates a conservative insertion-force demand and corresponding buckling margin. It is therefore intended to support structural selection and path screening before deployment.

The manipulator was successfully deployed in a nuclear decommissioning hot cell at NRS Dounreay, UK. The field operation confirmed the practicality of the proposed system and supported the applicability of the conservative stability envelope under real deployment conditions.

Future work will focus on enhancing the hardware capabilities of the system to further extend its operational performance. In particular, efforts will be directed towards increasing payload capacity, extending the achievable navigation distance, and improving lift-up height through advancements in structural stiffness and load-bearing design. These developments are also expected to improve robustness during deployment, especially when operating along more demanding paths that require higher insertion forces.

In addition, future research will investigate the behaviour of the long passive body under large-angle bending conditions, where configuration bifurcation and related instabilities may arise. Control strategies will be developed to identify and manage such configuration transitions during insertion and navigation, with the aim of ensuring stable and predictable deployment in complex environments.

Overall, the results indicate that reliable long-reach continuum deployment in hybrid industrial environments requires the joint consideration of structural design, conservative stability estimation, operational simplicity, and recovery planning. The proposed system and assessment approach provide a practical basis for future continuum manipulators operating in harsh industrial settings.

Acknowledgements. The authors would like to acknowledge the support received from the University of Nottingham; RAICo project; Game Changers project (GC651); and the UKRI RAIN + project (EP/W001128/1). The authors used AI-assisted tools

Downloaded from https://www.cambridge.org/core. UNIVERSIDAD AUTONOMA METROPOLITANA, on 16 Nov 2026 at 12:10:09, subject to the Cambridge Core terms of use, available at https://www.cambridge.org/core/terms. https://doi.org/10.1017/S0263574726103877

(ChatGPT) solely for English language editing and grammar checking. All scientific content, ideas, and conclusions are entirely the authors' own.

Author contributions. J.C. Chang conceived and designed the study. J.C. Chang, J. Liu, and H. Dai conducted data gathering. J.C. Chang performed statistical analyses. J.C. Chang, J. Liu, H. Dai, X. Wang, and D. Axinte wrote the article.

Financial support. The authors declare no financial support.

Competing interests. The authors declare no conflicts of interest exist.

Ethical standards. Not applicable.

References

[1] Z. Li, Y. Yang, X. Yu, C. Liu, O. Kaynak and H. Gao, "Fixed-time control of a novel thrust-vectoring aerial manipulator via high-order fully actuated system approach," *IEEE/ASME Trans. Mechatron.* **30**(2), 1084–1095 (2024).
[2] R. Almadhoun, T. Taha, L. Seneviratne, J. Dias and G. Cai, "A survey on inspecting structures using robotic systems," *Int. J. Adv. Robot. Syst.* **13**(6), 1729881416663664 (2016).
[3] X. Wang, S. Li, J.-C. Chang, J. Liu, D. Axinte and X. Dong, "Multimodal locomotion ultra-thin soft robots for exploration of narrow spaces," *Nat. Commun.* **15**(1), 6296 (2024).
[4] X. Dong, D. Axinte, D. Palmer, S. Cobos, M. Raffles, A. Rabani and J. Kell, "Development of a slender continuum robotic system for on-wing inspection/repair of gas turbine engines," *Robot. Cim-INT Manuf.* **44**, 218–229 (2017).
[5] W. Cheah, K. Groves, H. Martin, H. Peel, S. Watson, O. Marjanovic and B. Lennox, "MIRRAX: A reconfigurable robot for limited access environments," *IEEE Trans. Robot.* **39**(2), 1341–1352 (2022).
[6] W. Marquette, K. Schultz, V. Jonnalagadda, B. Wong, J. Garbini and S. Devasia, "Semi-autonomous teleoperation using differential flatness of a crane robot for aircraft in-wing inspection," *IEEE Robot. Autom. Lett.* **10**(3), 2742–2749 (2025).
[7] J. Fang, J. Xiang, L. Ma, H. Liu, C. Wang and S. Liang, "Gas-driven endoscopic robot for visual inspection of corrosion defects inside gas pipelines," *Processes.* **11**(4), 1098 (2023).
[8] M. Chiou, G.-T. Epsimos, G. Nikolaou, P. Pappas, G. Petousakis, S. Mühl and R. Stolkin. Robot-Assisted Nuclear Disaster Response: Report and Insights From a Field Exercise," **In:** *IEEE/RSJ International Conference on Intelligent Robots and Systems (IROS), IEEE* (2022) pp. 4545–4552.
[9] S. Kawatsuma, R. Mimura and H. Asama, "Unitization for portability of emergency response surveillance robot system: Experiences and lessons learned from the deployment of the JAEA-3 emergency response robot at the Fukushima Daiichi Nuclear Power Plants," *Robomech. J.* **4**(1), 6 (2017).
[10] S. Wang, K. Wang, R. Tang, J. Qiao, H. Liu and Z.-G. Hou, "Design of a low-cost miniature robot to assist the COVID-19 nasopharyngeal swab sampling," *IEEE Trans. Med. Robot. Bion.* **3**(1), 289–293 (2020).
[11] I. D. Gkegkes, I. A. Mamais and C. Iavazzo, "Robotics in general surgery: A systematic cost assessment," *J. Minim. Access Surg.* **13**(4), 243–255 (2017).
[12] M. Wang, X. Dong, W. Ba, A. Mohammad, D. Axinte and A. Norton, "Design, modelling and validation of a novel extra slender continuum robot for in-situ inspection and repair in aeroengine," *Robot. Cim-INT Manuf.* **67**, 102054 (2021).
[13] D. A. Troncoso, J. A. Robles-Linares, M. Russo, M. A. Elbanna, S. Wild, X. Dong, A. Mohammad, J. Kell, A. D. Norton and D. Axinte, "A continuum robot for remote applications: From industrial to medical surgery with slender continuum robots," *IEEE Robot. Autom. Mag.* **30**(3), 94–105 (2022).
[14] G. Niu, J. Wang and K. Xu, "Model analysis for a continuum aircraft fuel tank inspection robot based on the Rzeppa universal joint," *Adv. Mech. Eng.* **10**(5), 1687814018778229 (2018).
[15] L. Mao, P. Yang, C. Tian, X. Shen, F. Wang, H. Zhang, X. Meng and H. Xie, "Magnetic steering continuum robot for transluminal procedures with programmable shape and functionalities," *Nat. Commun.* **15**(1), 3759 (2024).
[16] Y. Yamauchi, Y. Ambe, H. Nagano, M. Konyo, Y. Bando, E. Ito, S. Arnold, K. Yamazaki, K. Itoyama, T. Okatani, H. G. Okuno and S. Tadokoro, "Development of a continuum robot enhanced with distributed sensors for search and rescue," *Robomech. J.* **9**(1), 8 (2022).
[17] I. D. Walker, H. Choset and G. S. Chirikjian, "Snake-Like and Continuum Robots," **In:** *Springer Handbook of Robotics*, Springer, (2016) pp. 481–498.
[18] J. Burgner-Kahrs, D. C. Rucker and H. Choset, "Continuum robots for medical applications: A survey," *IEEE Trans. Robot.* **31**(6), 1261–1280 (2015).
[19] M. Russo, S. M. H. Sadati, X. Dong, A. Mohammad, I. D. Walker, C. Bergeles, K. Xu and D. A. Axinte, "Continuum robots: An overview," *Adv. Intell. Syst.* **5**(5), 2200367 (2023).
[20] N. Simaan, R. Taylor and P. Flint. A Dexterous System for Laryngeal Surgery," **In:** *IEEE International Conference on Robotics and Automation, 2004. Proceedings. ICRA04*, IEEE, **1**, (2004) pp. 351–357.
[21] R. J. Webster III. *Design and Mechanics of Continuum Robots for Surgery* (The Johns Hopkins University ProQuest Dissertations & Theses, 3309778, 2008).
[22] N. Kumar, "Are continuum robots the future of advanced manufacturing?," *Adv. Robot. Manuf.* (2023), chapter 7 (online).

Downloaded from https://www.cambridge.org/core. UNIVERSIDAD AUTONOMA METROPOLITANA, on 16 Nov 2026 at 12:10:09, subject to the Cambridge Core terms of use, available at https://www.cambridge.org/core/terms. https://doi.org/10.1017/S0263574726103877

[23] N. Ma, S. Monk and D. Cheneler, "Collaborative continuum robots for remote engineering operations," *Biomimetics.* **8**(1), 4 (2022).
[24] C. McFarland, A. Dhawan, R. Kumari, C. Council, M. Coad and N. Hanson. "Field insights for portable vine robots in urban search and rescue," **In:** *IEEE International Symposium on Safety Security Rescue Robotics (SSRR), 2024: IEEE* (2024) pp. 190–197.
[25] G. Li, J. Yu, D. Dong, J. Pan, H. Wu, S. Cao, X. Pei, X. Huang and J. Yi, "Systematic design of a 3-DOF dual-segment continuum robot for in situ maintenance in nuclear power plants," *Machines.* **10**(7), 596 (2022).
[26] C. Bishop, M. Russo, X. Dong and D. Axinte, "A novel underactuated continuum robot with shape memory alloy clutches," *IEEE/ASME Trans. Mechatron.* **27**(6), 5339–5350 (2022).
[27] J. Starke, E. Amanov, M. T. Chikhaoui and J. Burgner-Kahrs. On the merits of helical tendon routing in continuum robots," **In:** *IEEE/RSJ International Conference on Intelligent Robots and Systems (IROS), IEEE*, (2017) pp. 6470–6476.
[28] R. Kang, E. Guglielmino, L. Zullo, D. T. Branson, I. Godage and D. G. Caldwell, "Embodiment design of soft continuum robots," *Adv. Mech. Eng.* **8**(4), 1687814016643302 (2016).
[29] J.-A. Long, P. Cinquin, J. Troccaz, S. Voros, P. Berkelman, J.-L. Descotes, C. Letoublon and J.-J. Rambeaud, "Development of miniaturized light endoscope-holder robot for laparoscopic surgery," *J. Endourol.* **21**(8), 911–914 (2007).
[30] S.-H. Kim, H.-S. Choi, B. Keum and H.-J. Chun, "Robotics in gastrointestinal endoscopy," *Appl. Sci.* **11**(23), 11351 (2021).
[31] T. Takamatsu, Y. Endo, R. Fukushima, T. Yasue, K. Shinmura, H. Ikematsu and H. Takemura, "Robotic endoscope with double-balloon and double-bend tube for colonoscopy," *Sci. Rep.* **13**(1), 10494 (2023).
[32] H. Yamamoto, Y. Sekine, Y. Sato, T. Higashizawa, T. Miyata, S. Iino, K. Ido and K. Sugano, "Total enteroscopy with a nonsurgical steerable double-balloon method," *Gastrointest. Endosc.* **53**(2), 216–220 (2001).
[33] M. A. Atalla, F. Trauzettel, S. P. van Gelder, P. Breedveld, M. Wiertlewski and A. Sakes, "Mechanically-Inflatable Bio-Inspired Locomotion for Robotic Pipeline Inspection," **In:** *IEEE. 7th International Conference on Soft Robotics (RoboSoft), IEEE*, (2024) pp. 586–592.
[34] E. Y. Yarbasi and E. Samur, "Design and evaluation of a continuum robot with extendable balloons," *Mech. Sci.* **9**(1), 51–60 (2018).
[35] J.-C. Chang, H. Dai, X. Wang, D. Axinte and X. Dong, "Development of a continuum robot with inflatable stiffness-adjustable elements for in-situ repair of aeroengines," *Robot. Cim-INT Manuf.* **95**, 103018 (2025).
[36] G. Greenhill, "Determination of the greatest height consistent with stability that a vertical pole or mast can be made, and the greatest height to which a tree of given proportions can grow," **In:** *Proceedings of the Cambridge Philosophical Society*, (1881) vol. **4**, pp. 65.
[37] H. Baek, B. Cheon, J. M. You and D.-S. Kwon, "Design and analysis of feeder mechanism for buckling prevention in robotic catheterization," *J. Comput. Design Eng.* **9**(4), 1467–1481 (2022).
[38] F. Boyer, V. Lebastard, F. Candelier, F. Renda and M. Alamir, "Statics and dynamics of continuum robots based on Cosserat rods and optimal control theories," *IEEE Trans. Robot.* **39**(2), 1544–1562 (2022).
[39] J. Miller, T. Su, J. Pabon, N. Wicks, K. Bertoldi and P. Reis, "Buckling-induced lock-up of a slender rod injected into a horizontal cylinder," *Int. J. Solids Struct.* **72**, 153–164 (2015).
[40] S. P. Timoshenko and J. M. Gere. *Theory of Elastic Stability* (Dover Publications, Mineola, NY, 2012).
[41] J. H. Bickford. *Introduction to the Design and Behavior of Bolted Joints: Non-Gasketed Joints*, 4th ed. (CRC press, Boca Raton, 2007).
[42] K. Bisshopp and D. C. Drucker, "Large deflection of cantilever beams," *Quart. Appl. Math.* **3**(3), 272–275 (1945).

Cite this article: J.-C. Chang, J. Liu, H. Dai, X. Wang, D. Axinte and X. Dong (2026). "Development of extra-long continuum manipulator for nuclear facility inspection", Robotica **44**, 2070–2087. https://doi.org/10.1017/S0263574726103877

Downloaded from https://www.cambridge.org/core. UNIVERSIDAD AUTONOMA METROPOLITANA, on 16 Nov 2026 at 12:10:09, subject to the Cambridge Core terms of use, available at https://www.cambridge.org/core/terms. https://doi.org/10.1017/S0263574726103877